Bettingen BS (SBEG)

SITE CHARACTERIZATION REPORT

Clotaire MICHEL, Daniel ROTEN, Valerio POGGI,

Jan BURJANEK, Carlo CAUZZI, Donat FÄH

Sonneggstrasse 5 CH-8092 Zürich Switzerland; E-mail: `clotaire.michel@sed.ethz.ch`

Last modified : November 5, 2013

Abstract

The new station SBEG of the Swiss Strong Motion Network located in Bettingen, on the rock hills above the Rhine basin in Basel, is replacing a dial-up station. In order to characterize the velocity profile under the station, array measurements were reprocessed. The H/V analysis showed a fundamental frequency at $4.0\,\mathrm{Hz}$ due to a $18\,\mathrm{m}$ deep layer of loose alluvium with $V_s = 350\,\mathrm{m/s}$ on top of more consolidated sediments with the bedrock at $30 - 40\,\mathrm{m}$. A deep resonance within the rock at $0.5\,\mathrm{Hz}$ was found but was too deep too be interpreted in terms of velocity profile. $V_{s,30}$ is found to be close to $450\,\mathrm{m/s}$, which hardly makes it a rock reference. The theoretical SH transfer function and impedance contrast of the quarter-wavelength velocity computed from the inverted profiles show a large amplification up to 5 at the resonance frequencies, especially at $4.0\,\mathrm{Hz}$. Recordings on the new station will allow to validate these simple models.

Contents

1 Introduction

The station SBEG (Bettingen) of the Swiss Strong Motion Network (SSMNet) is the rock reference for the Basel network. SBEG has been renewed in the framework of the SSMNet Renewal project in 2012, replacing a dial-up station (Fig. 1). This project includes also the site characterization. The passive array measurement has been selected as a standard tool to investigate these sites. In Bettingen, a measurement campaign had already been carried out in 2005 by Havenith and Fäh [2006], with centre at station SBEG, in order to characterize the soil column under this station. According to the geological map, this station is located on recent alluvium and rock mass from the surrounding hills on top of Muschelkalk (limestone) rock. This report presents briefly the measurement setup, the results of the H/V analysis and of the array processing of the surface waves (dispersion curves). Then, an inversion of these results for a velocity profile is performed. Standard parameters are derived to evaluate the amplification at this site.

Canton	City	Location	Station code	Site type	Slope
Basel Stadt	Bettingen	Centre	SBEG	Rock hill	$\geq 15\,^\circ$

Table 1: Main characteristics of the study-site.

Figure 1: Picture of the site.

2 Experiment description

2.1 Ambient Vibrations

The ground surface is permanently subjected to ambient vibrations due to:

- natural sources (ocean and large-scale atmospheric phenomena) below $1\,\mathrm{Hz}$,

- local meteorological conditions (wind and rain) at frequencies around $1\,\mathrm{Hz}$,

- human activities (industrial machines, traffic...) at frequencies above $1\,\mathrm{Hz}$ [Bonnefoy-Claudet et al., 2006].

The objective of the measurements is to record these ambient vibrations and to use their propagation properties to infer the underground structure. First, the polarization of the recorded waves (H/V ratio) is used to derive the resonance frequencies of the soil column. Second, the phase delays at many different stations are used to derive the velocity of surface waves at different frequencies (dispersion). The information (H/V, dispersion curves) is then used to derive the properties of the soil column using an inversion process.

2.2 Equipment

For this array measurements, 5 Quanterra Q330 dataloggers named NR1 to NR5 and 10 Lennartz 3C 5 s seismometers were used. Each datalogger can record on 2 ports A (channels EH1, EH2, EH3 for Z, N, E directions) and B (channels EH4, EH5, EH6 for Z, N, E directions). Time synchronization was ensured by GPS.

2.3 Geometry of the arrays

The two array configurations performed by H.-B. Havenith were used. The first configuration has a $60\,\mathrm{m}$ aperture with 9 sensors; the second configuration has a $160\,\mathrm{m}$ with 10 sensors. The experimental setup is displayed in Fig. 2. The final usable datasets are detailed in section 3.2.

2.4 Positioning of the stations

Positioning of the stations was performed by H.-B. Havenith using a theodolite, ensuring a relative precision better than $1\,\mathrm{cm}$, but a poor absolute precision on the Swissgrid, because the reference point was not set accurately, so that some points are located on buildings on Fig. 2.
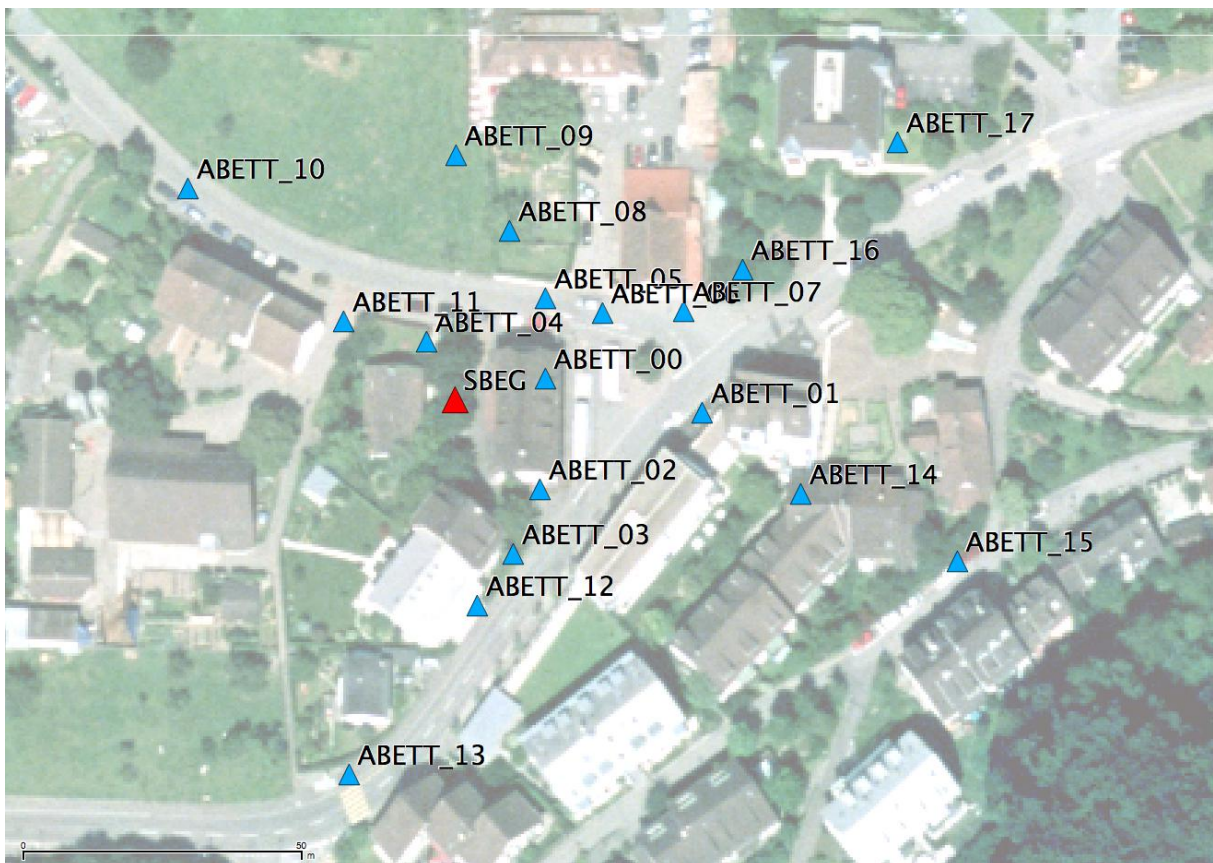
Figure 2: Geometry of the arrays.

3 Data quality

3.1 Usable data

The largest time windows were extracted, for which the GPS synchronization was ensured for all stations. Orientation of the sensor was checked by maximizing the correlation with the central station at low frequencies (between 1 and $3\,\mathrm{Hz}$ here) [Poggi et al., 2012b]. Deviation of $15\,^{\circ}$ was found for ABETT_14 and $\pm 10\,^{\circ}$ at points ABETT_01, ABETT_02 and ABETT_17, much lower at the other points. Original and rotated datasets are available for the array analysis. The characteristics of the datasets are detailed in Tab. 2.

3.2 Data processing

In order to be re-processed, the raw data were first converted to SAC format including in the header the sensor coordinates (CH1903 system), the recording component and a name related to the position. The name is made of letters characterizing the location (ABETT here) and 2 digits from 00 to 17. Recordings were not corrected from the instrument response.

Dataset	Starting Date	Time	Length	F_s	Min. inter-distance	Aperture	# of points
1	2005/04/22	8:00	77 min	200 Hz	15 m	60 m	9
2	2005/04/22	10:21	52 min	200 Hz	40 m	160 m	10

Table 2: Usable datasets.

4   H/V processing

4.1   Processing method and parameters

In order to process the H/V spectral ratios, several codes and methods were used. The classical H/V method was applied using the Geopsy `http://www.geopsy.org` software. In this method, the ratios of the smoothed Fourier Transform of selected time windows are averaged. Tukey windows (cosine taper of 5% width) of $100\,\mathrm{s}$ long overlapping by 50% were selected. Konno and Ohmachi [1998] smoothing procedure with b=60 was used. The classical H/V method of Fäh et al. [2001] was also applied.

Moreover, the time-frequency analysis method [Fäh et al., 2009] was used to estimate the ellipticity function more accurately using the Matlab code of V. Poggi. In this method, the time-frequency analysis using the Wavelet transform is computed for each component. For each frequency, the maxima over time (10 per minute with at least $0.1\,\mathrm{s}$ between each) in the TFA are determined. The Horizontal to Vertical ratio of amplitudes for each maxima is then computed and statistical properties for each frequency are derived. Cosine wavelet with parameter 9 was used. The mean of the distribution for each frequency is stored. For the sake of comparison, the time-frequency analysis of Fäh et al. [2001], based on the spectrogram, was also used, as well as the wavelet-based TFA coded in Geopsy.

The ellipticity extraction using the Capon analysis [Poggi and Fäh, 2010] on the array measurement was also performed (see section 5).

Method	Freq. band	Win. length	Anti-trig.	Overlap	Smoothing
Standard H/V Geopsy	$0.2 - 20\,\mathrm{Hz}$	$100\,\mathrm{s}$	No	50%	K&O 60
Standard H/V D. Fäh	$0.2 - 20\,\mathrm{Hz}$	$30\,\mathrm{s}$	No	75%	-
H/V TFA Geopsy	$0.2 - 20\,\mathrm{Hz}$	Morlet m=8 fi=1	No	-	-
H/V TFA D. Fäh	$0.2 - 20\,\mathrm{Hz}$	Specgram	No	-	-
H/V TFA V. Poggi	$0.2 - 20\,\mathrm{Hz}$	Cosine wpar=9	No	-	No

Table 3: Methods and parameters used for the H/V processing.

4.2   Results

H/V curves are consistent for all the recordings in the array (Fig. 3), showing a slight variability. Moreover, all the methods to compute H/V ratios are compared on Fig. 4, where the classical methods were divided by $\sqrt{2}$ to correct from Love waves influence [Fäh et al., 2001]. All methods provide similar results, except that the position of the peak may be slightly shifted. The 3C FK analysis provides similar results as well but is not able to explore the part related to the fundamental frequency due to the too small array aperture compared to the basin depth. The peak is relatively clear around $4.0\,\mathrm{Hz}$, with a peak amplitude around 2.5. A spurious frequency at $4.5\,\mathrm{Hz}$ may affect the picking. Moreover, a low frequency resonance at about $0.5\,\mathrm{Hz}$ can be seen but is related to a too deep structure, within the rock, to be used in the following.
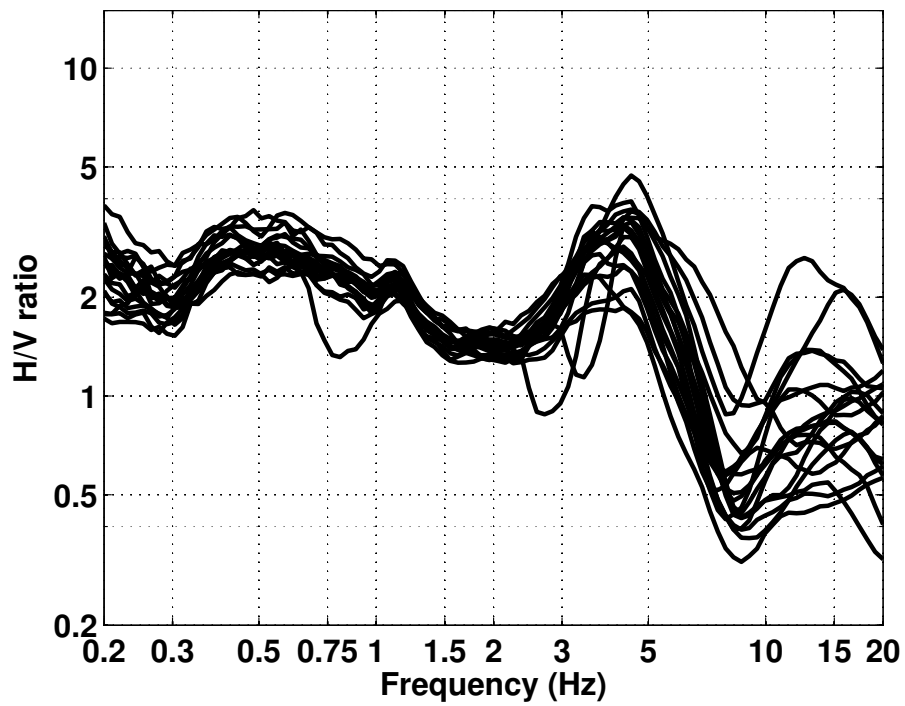
Figure 3: H/V spectral ratios (time-frequency analysis code V. Poggi).
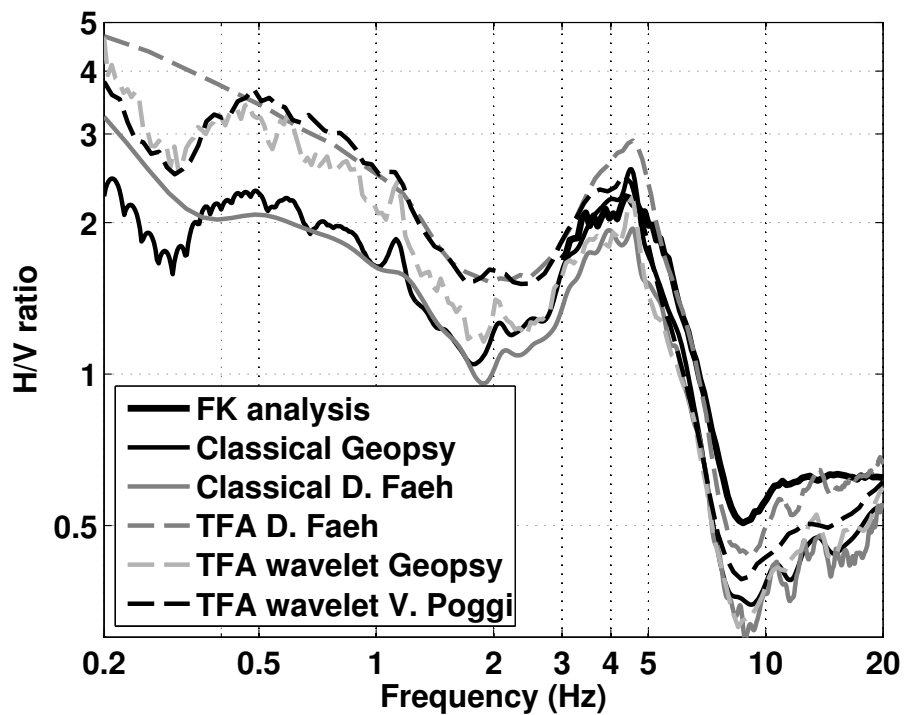
Figure 4: H/V spectral ratios for point ABETT_00 using the different codes. Classical methods were divided by $\sqrt{2}$.

5   Array processing

5.1   Processing methods and parameters

The 3C array analysis [Fäh et al., 2008] was performed using the array_tool_3C software [Poggi and Fäh, 2010]. The results of computations of both datasets were merged to estimate the dispersion curves. It allows to derive Rayleigh and Love modes. Original and rotated datasets were processed.

The array was also processed following the method proposed in Maranò et al. [2012]. Results are obtained jointly modeling up to three propagating plane waves at each time window and frequency. The method models both Rayleigh and Love waves. The recording is split in windows of 20 seconds. Parameter estimation is done via maximum likelihood considering jointly all the measurement from three components sensors. Wavefield parameters estimated include wavenumber, azimuth, and Rayleigh wave ellipticity. Model selection (choice of wave type and number of waves) is performed using the Bayesian information criterion.

Method	Set	Freq. band	Win. length	Anti-trig.	Overlap	Grid step	Grid size	# max.
HRFK 3C	1	$3 - 30\,\mathrm{Hz}$	Wav. 10 Tap. 0.2	No	50%	200 m/s	2500 m/s	5
HRFK 3C	2	$3 - 30\,\mathrm{Hz}$	Wav. 10 Tap. 0.2	No	50%	200 m/s	2500 m/s	5
Waveform decomp.	1	$0 - 20\,\mathrm{Hz}$	20s					
Waveform decomp.	2	$0 - 20\,\mathrm{Hz}$	20s					

Table 4: Methods and parameters used for the array processing.

5.2   Obtained dispersion curves

Both fundamental Rayleigh and Love modes can be picked as well as the first Love higher mode (Fig. 5). Results following the wavefield decomposition method are also similar both using 1 or 3 waves for the modelling (Fig. 7). The fundamental Rayleigh mode is comparable to the initial array processing by Havenith, although the array limit was not respected by this previous computation (Fig. 7). Rayleigh fundamental mode is picked from 4.3 to $26\,\mathrm{Hz}$ and Love from 4 to $17\,\mathrm{Hz}$ (Fig. 8).

Rotated datasets (Fig. 6) provide better results in the sense that only Rayleigh mode appears on the radial component, making the picking easier. However, no deviation was noticed neither in the dispersion curves, nor in the ellipticity.

The ellipticity results (Fig. 9) show however large differences between classical and FK based approach and the wave-field decomposition method. This last method shows a much steeper curve with higher peak which is compatible with the inversions, on the contrary to the classical H/V curves. The peak is however not well defined due to the low array aperture.
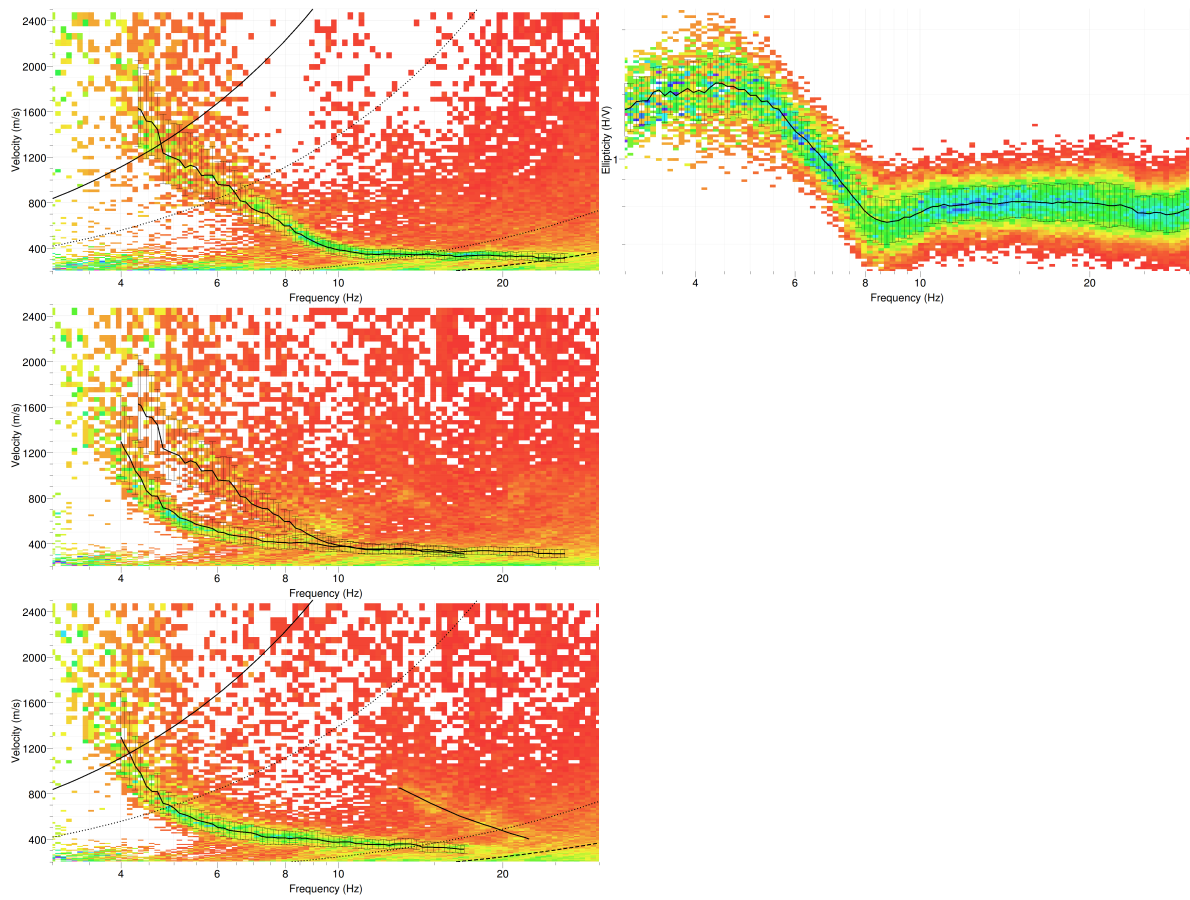
Figure 5: Dispersion curves obtained from the 3C array analysis with original data: vertical direction dispersion and ellipticity (top), radial direction (centre) and transverse direction (bottom).
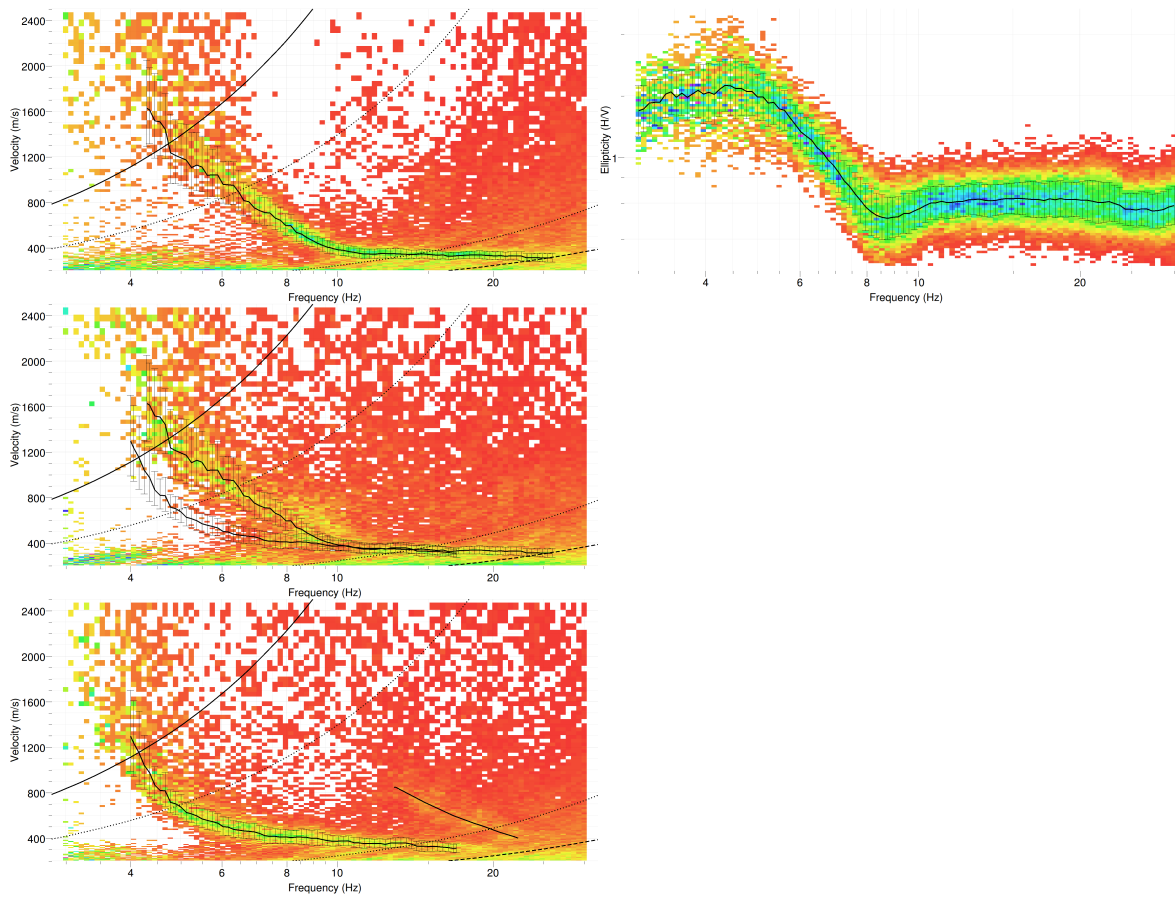
Figure 6: Dispersion curves obtained from the 3C array analysis with realigned (rotated) data: vertical direction dispersion and ellipticity (top), radial direction (centre) and transverse direction (bottom).
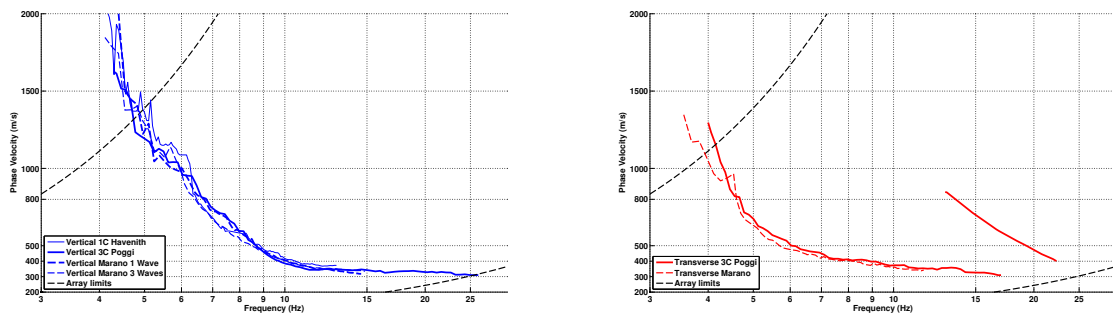
Figure 7: Picked dispersion curves using the different methods in the Vertical (left) and Transverse (right) components.
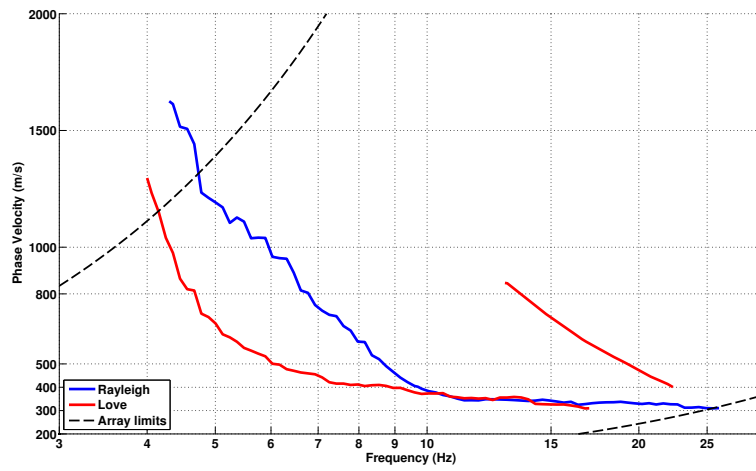
Figure 8: Selected dispersion curves.
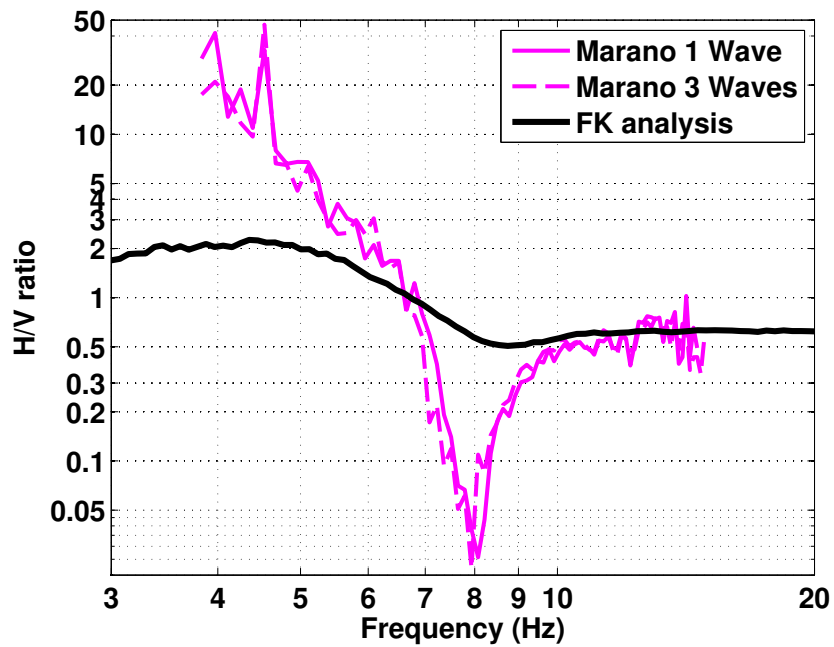
Figure 9: Picked ellipticity curves with the array processing methods.

6   Inversion and interpretation

6.1   Inversion

For the inversion, the Love and Rayleigh fundamental modes and Love first higher mode dispersion curves between 4 and $25\,\mathrm{Hz}$ were used as simultaneous targets without standard deviation to avoid different weighting as well as the ellipticity curve obtained by the wavefield decomposition method between 4 and $12\,\mathrm{Hz}$. A weight of 0.15 was assigned to the ellipticity curve. All curves were resampled using 50 points between 3 and $30\,\mathrm{Hz}$ in log scale.

The inversion was performed using the Improved Neighborhood Algorithm (NA) [Wathelet, 2008] implemented in the Dinver software. In this algorithm, the tuning parameters are the following: Ns_0 is the number of starting models, randomly distributed in the parameter space, Nr is the the number of best cells considered around these Ns_0 models, Ns is the number of new cells generated in the neighborhood of the Nr cells (Ns/Nr per cell) and It_{max} is the number of iteration of this process. The process ends with $Ns_0 + Nr * \frac{Ns}{Nr} * It_{max}$ models. The used parameters are detailed in Tab. 5.

It_{max}	Ns_0	Ns	Nr
500	10000	100	100

Table 5: Tuning parameters of Neighborhood Algorithm.

During the inversion process, low velocity zones were not allowed. The Poisson ratio was inverted in each layer in the range 0.2-0.45 and the density was supposed equal to $2000\,\mathrm{kg/m}^3$ except for the layers assumed to be rock ($2500\,\mathrm{kg/m}^3$). Inversions with free layer depths as well as fixed layer depths were performed. 3 layers are enough to explain most of the targets (dispersion and ellipticity), but more layers are used to smooth the obtained results and better explore the parameter space. 5 independent runs of 5 different parametrization schemes (3 and 5 layers over a half space, see Fig. 10 and 7, 9 and 11 layers with fixed depth, see Fig. 11) were performed. For further elaborations, the best models of these 25 runs were selected (Fig. 12).

The maximum velocity in the rock was set to $2500\,\mathrm{m/s}$ based on a priori knowledge [Fäh et al., 2006]. The velocity profile shows a clear layer from the surface down to $18\,\mathrm{m}$ with a well defined velocity of about $350\,\mathrm{m/s}$. Below, down to $30 - 40\,\mathrm{m}$, the velocity increases gradually up to $1000\,\mathrm{m/s}$. The bedrock is found at $30 - 40\,\mathrm{m}$ with a sharp velocity contrast. The velocity in the bedrock is hardly constrained, however.

When compared to the target curves (Fig. 10), the Love and Rayleigh modes are well reproduced as well as the ellipticity from the wave field decomposition method. It should be noticed that the ellipticity curve from other methods could not be used in the inversion here. The peak ellipticity is found at the right frequency compared to H/V curves.

Looking at the geological map, rock has a $26\,^\circ$ slope. Assuming this angle is constant below the alluvium, one can interpolate the depth of the alluvium. It would then be $35\,\mathrm{m}$ deep at the array centre, which is coherent with what was found here.
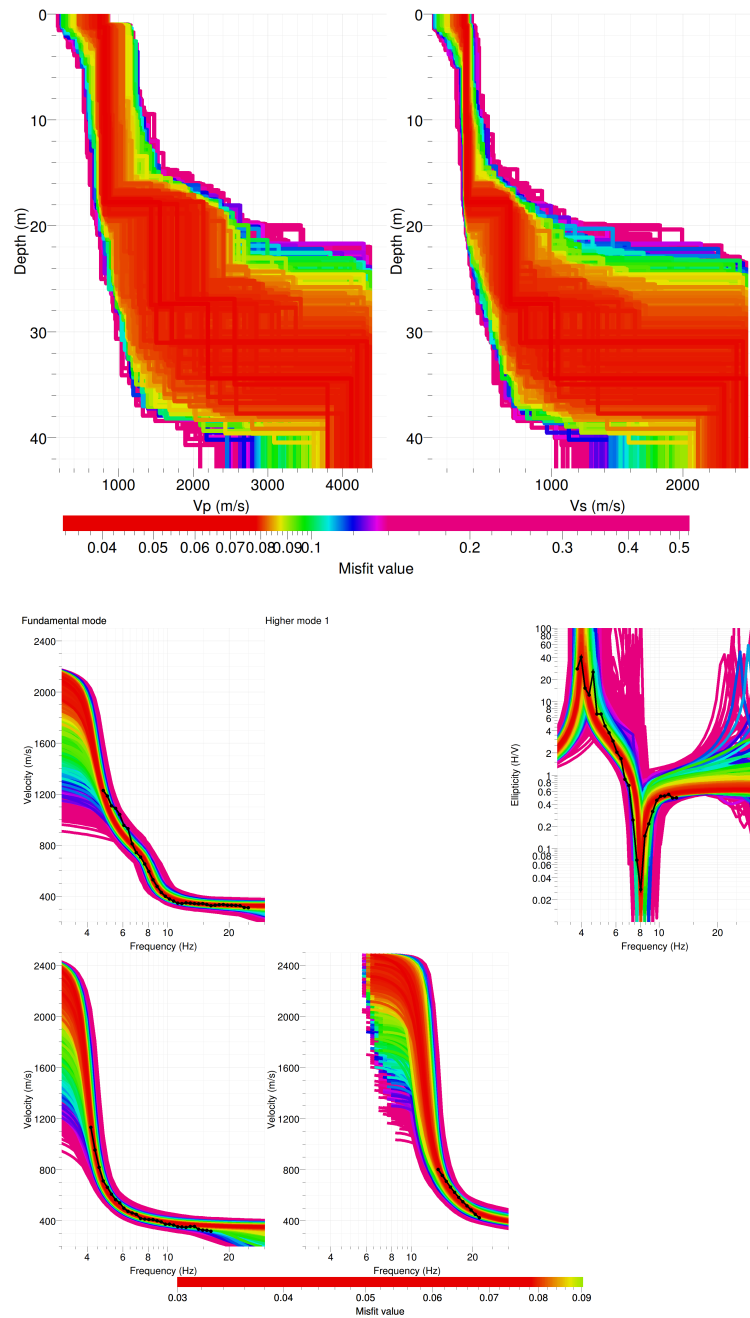
Figure 10: Inverted ground profiles in terms of V_p and V_s (top) and comparison between inverted models and measured Rayleigh and Love modes and corresponding ellipticity, free layer depth strategy.
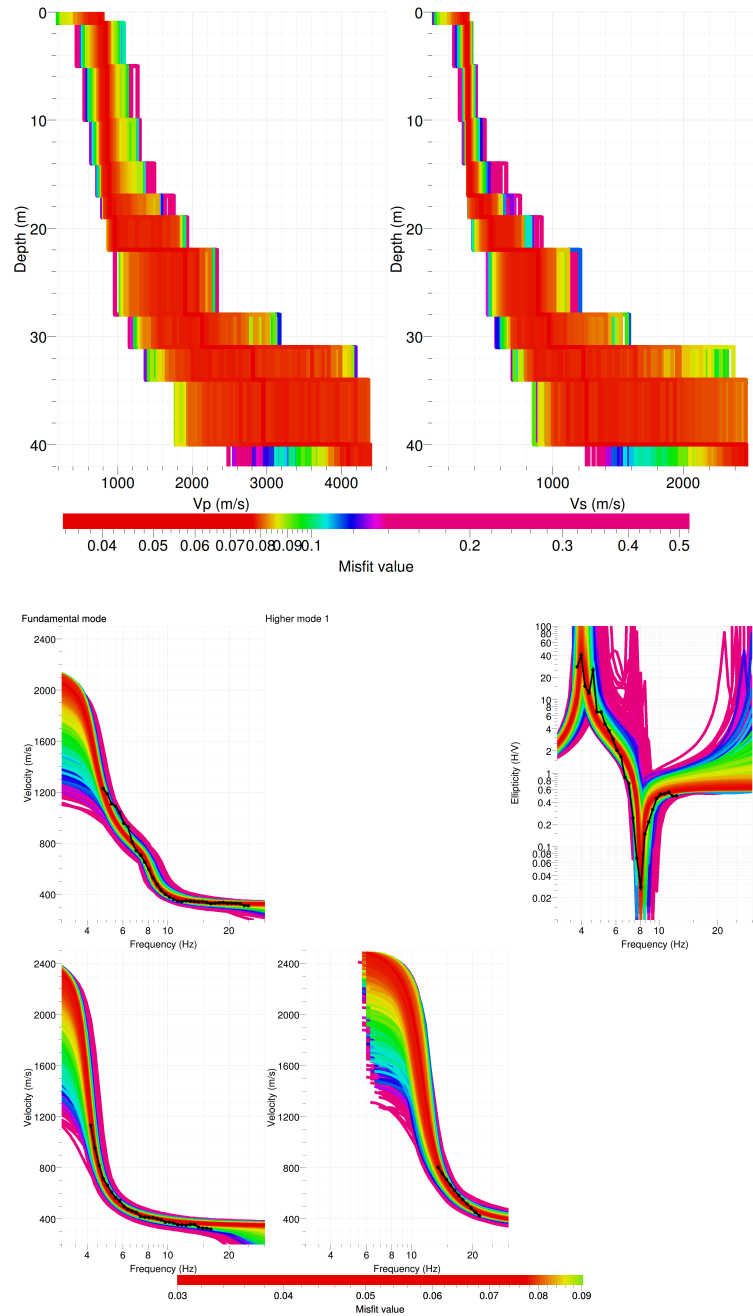
Figure 11: Inverted ground profiles in terms of V_p and V_s (top) and comparison between inverted models and measured Rayleigh and Love modes and corresponding ellipticity, fixed layer depth strategy.
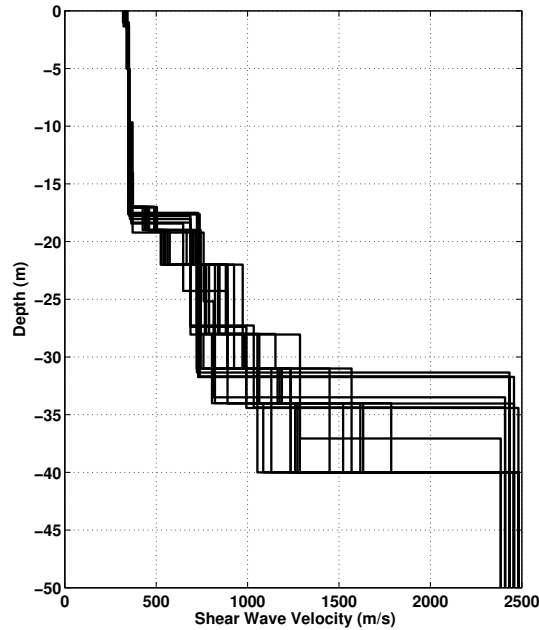
Figure 12: V_s ground profiles for the selected 25 best models (fixed and free depth strategies).

6.2 Travel time average velocities and ground type

The distribution of the travel time average velocities at different depths was computed from the selected models. The uncertainty, computed as the standard deviation of the distribution of travel time average velocities for the considered models, is also provided, but its meaning is doubtful. $V_{s,30}$ is found to be $444\,\mathrm{m/s}$, meaning the site can be classified as type B, at the limit with type E, in the Eurocode 8 [CEN, 2004] and in type E in SIA261 [SIA, 2003]. For SIA261, the first $18\,\mathrm{m}$ at $350\,\mathrm{m/s}$ on top of better consolidated sediments with $V_s > 400\,\mathrm{m/s}$ would correspond to type E. Although the velocity contrast remains low, it would probably be the choice made by an engineer. Concerning EC8, the required velocity contrast for type E is larger: it needs a $V_s > 800\,\mathrm{m/s}$ which is found around $30\,\mathrm{m}$, at the upper limit for type E. Moreover, the velocity of the sediments above this limit is at the upper bound for type E ($V_s < 360\,\mathrm{m/s}$).

6.3 SH transfer function and quarter-wavelength velocity

The quarter-wavelength velocity approach [Joyner et al., 1981] provides, for a given frequency, the average velocity at a depth corresponding to 1/4 of the wavelength of interest. It is useful to identify the frequency limits of the experimental data (minimum frequency in ellipticity and dispersion curves, $4\,\mathrm{Hz}$ here). The results using this proxy show that no data is controlling the results below $25\,\mathrm{m}$, i.e. the bedrock properties (Fig. 13). Moreover, the quarter wavelength impedance-contrast introduced by Poggi et al. [2012a] is also displayed in the figure. It corresponds to the ratio between two quarter-wavelength average velocities, respectively from the top and the bottom part of the velocity profile, at a given frequency [Poggi et al., 2012a]. It

	Mean (m/s)	Uncertainty (m/s)
$V_{s,5}$	342	3
$V_{s,10}$	346	2
$V_{s,20}$	368	2
$V_{s,30}$	444	3
$V_{s,40}$	508	30
$V_{s,50}$	575	50
$V_{s,100}$	-	-
$V_{s,150}$	-	-
$V_{s,200}$	-	-

Table 6: Travel time averages at different depths from the inverted models. Uncertainty is given as one standard deviation from the selected profiles.

shows a trough (inverse shows a peak) at the resonance frequency.

Moreover, the theoretical SH-wave transfer function for vertical propagation [Roesset, 1970] is computed from the inverted profiles. It is compared to the quarter-wavelength amplification [Joyner et al., 1981], that however cannot take resonances into account (Fig. 14). In this case, the models are predicting an amplification up to a factor of 7 at the fundamental frequency around $4\,\mathrm{Hz}$ as well as for upper modes above $10\,\mathrm{Hz}$. This will be compared to observations at this station.
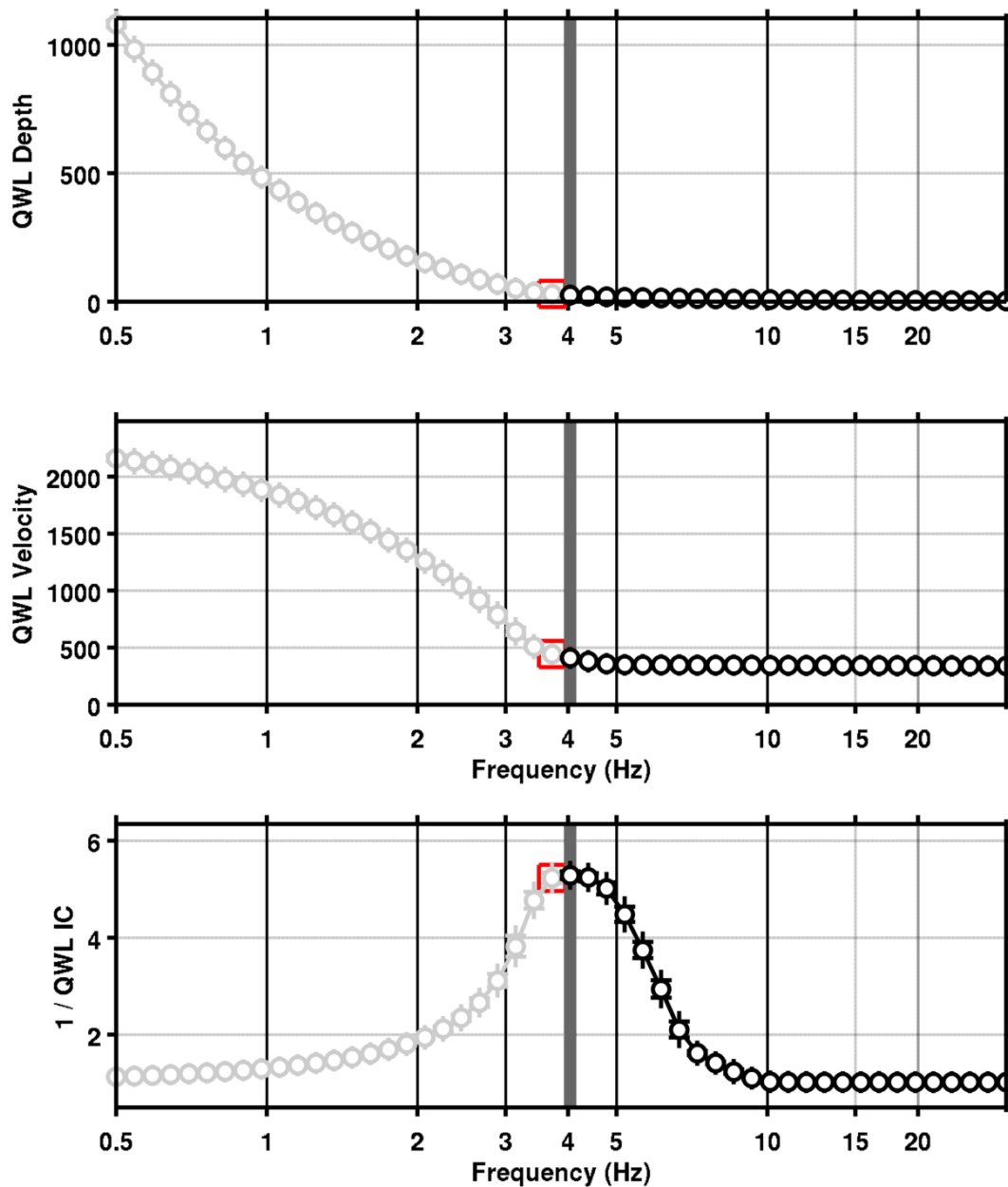
Figure 13: Quarter wavelength velocity representation of the velocity profile (top: depth, centre: velocity, bottom: inverse of the impedance contrast). Black curve is constrained by the dispersion curves, light grey is not constrained by the data. Red square is corresponding to $V_{s,30}$.
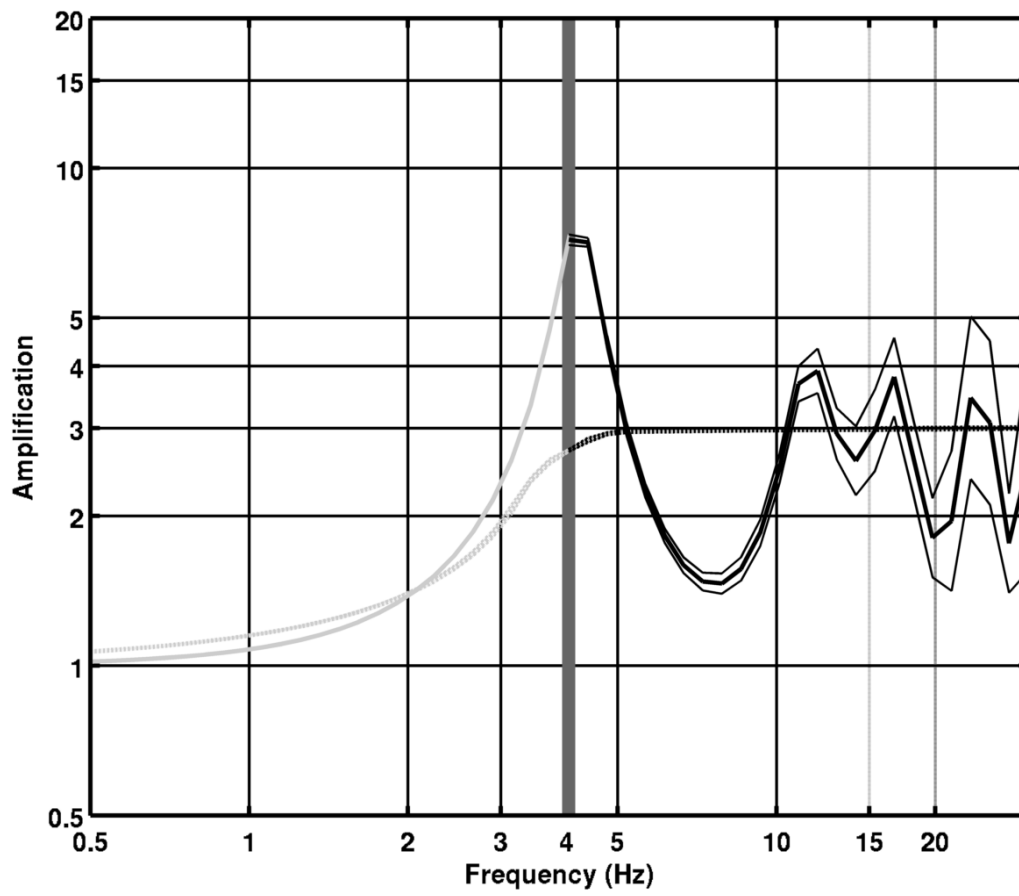
Figure 14: Theoretical SH transfer function (solid line) and quarter wavelength impedance contrast (dashed line) with their standard deviation. Significance of the greyshades is detailed in Fig. 13.

7 Conclusions

The array measurements re-processed in this study were successful in deriving a velocity model below the SBEG station. We found a $18\,\mathrm{m}$ sedimentary layer with $V_s = 350\,\mathrm{m/s}$ on more consolidated sediments and the bedrock at $30 - 40\,\mathrm{m}$, with an unconstrained velocity. A deep resonance within the rock at $0.5\,\mathrm{Hz}$ was found but was too deep too be interpreted in terms of velocity profile. $V_{s,30}$ is found to be close to $450\,\mathrm{m/s}$, which hardly makes it considered as a rock site. The theoretical SH transfer function and impedance contrast of the quarter-wavelength velocity computed from the inverted profiles show a large amplification up to 5 at the resonance frequencies, especially at the fundamental frequency at $4\,\mathrm{Hz}$. Recordings on the new station will allow to validate these simple models.

Acknowledgements

References

Sylvette Bonnefoy-Claudet, Fabrice Cotton, and Pierre-Yves Bard. The nature of noise wavefield and its applications for site effects studies. *Earth-Science Reviews*, 79(3-4): 205–227, December 2006. ISSN 00128252. doi: 10.1016/j.earscirev.2006.07.004. URL http://linkinghub.elsevier.com/retrieve/pii/S0012825206001012.

CEN. *Eurocode 8: Design of structures for earthquake resistance - Part 1: General rules, seismic actions and rules for buildings*. European Committee for Standardization, en 1998-1: edition, 2004.

Donat Fäh, Fortunat Kind, and Domenico Giardini. A theoretical investigation of average H / V ratios. *Geophysical Journal International*, 145:535–549, 2001.

Donat Fäh, Brian Steiner, Hans Havenith, Sibylle Steimen, Peter Huggenberger, and Erich Fäh. INTERREG III Projekt: Erdbebenmikrozonierung am südlichen Oberrhein. Teilbericht 1: Zoneneinteilung. Technical report, Eidgenössische Technische Hochschule Zürich (ETHZ), 2006.

Donat Fäh, Gabriela Stamm, and Hans-Balder Havenith. Analysis of three-component ambient vibration array measurements. *Geophysical Journal International*, 172(1):199–213, January 2008. ISSN 0956540X. doi: 10.1111/j.1365-246X.2007.03625.x. URL http://doi. wiley.com/10.1111/j.1365-246X.2007.03625.x.

Donat Fäh, Marc Wathelet, Miriam Kristekova, Hans-Balder Havenith, Brigitte Endrun, Gabriela Stamm, Valerio Poggi, Jan Burjanek, and Cécile Cornou. Using Ellipticity Information for Site Characterisation Using Ellipticity Information for Site Characterisation. Technical report, NERIES JRA4 Task B2, 2009.

Hans-Balder Havenith and Donat Fäh. INTERREG III Projekt: Erdbebenmikrozonierung am südlichen Oberrhein. Teilbericht 2: Bestimmung der Scherwellengeschwindigkeiten. Technical report, Eidgenössische Technische Hochschule Zürich (ETHZ), 2006.

William B. Joyner, Richard E. Warrick, and Thomas E. Fumal. The effect of Quaternary alluvium on strong ground motion in the Coyote Lake, California, earthquake of 1979. *Bulletin of the Seismological Society of America*, 71(4):1333–1349, 1981.

Katsuaki Konno and Tatsuo Ohmachi. Ground-Motion Characteristics Estimated from Spectral Ratio between Horizontal and Vertical Components of Microtremor. *Bulletin of the Seismological Society of America*, 88(1):228–241, 1998.

Stefano Maranò, C. Reller, H.-A. Loeliger, and Donat Fäh. Seismic waves estimation and wave field decomposition: Application to ambient vibrations. *Geophysical Journal International*, submitted, 2012.

Valerio Poggi and Donat Fäh. Estimating Rayleigh wave particle motion from three-component array analysis of ambient vibrations. *Geophysical Journal International*, 180(1):251–267, January 2010. ISSN 0956540X. doi: 10.1111/j.1365-246X.2009.04402.x. URL http: //doi.wiley.com/10.1111/j.1365-246X.2009.04402.x.

Valerio Poggi, Benjamin Edwards, and D. Fah. Characterizing the Vertical-to-Horizontal Ratio of Ground Motion at Soft-Sediment Sites. *Bulletin of the Seismological Society of America*, 102(6):2741–2756, December 2012a. ISSN 0037-1106. doi: 10.1785/0120120039. URL `http://www.bssaonline.org/cgi/doi/10.1785/0120120039`.

Valerio Poggi, Donat Fäh, Jan Burjanek, and Domenico Giardini. The use of Rayleigh-wave ellipticity for site-specific hazard assessment and microzonation: application to the city of Lucerne, Switzerland. *Geophysical Journal International*, 188(3):1154–1172, March 2012b. ISSN 0956540X. doi: 10.1111/j.1365-246X.2011.05305.x. URL `http://doi.wiley.com/10.1111/j.1365-246X.2011.05305.x`.

J.M. Roesset. Fundamentals of soil amplification. In R. J. Hansen, editor, *Seismic Design for Nuclear Power Plants*, pages 183–244. M.I.T. Press, Cambridge, Mass., 1970. ISBN 978-0-262-08041-5. URL `http://mitpress.mit.edu/catalog/item/default.asp?ttype=2\&tid=5998`.

SIA. *SIA 261 Actions sur les structures porteuses*. Société suisse des ingénieurs et des architectes, Zürich, sia 261:20 edition, 2003.

Marc Wathelet. An improved neighborhood algorithm: Parameter conditions and dynamic scaling. *Geophysical Research Letters*, 35(9):1–5, May 2008. ISSN 0094-8276. doi: 10.1029/2008GL033256. URL `http://www.agu.org/pubs/crossref/2008/2008GL033256.shtml`.